Multiscale Damage Analyses of Red Sandstone in Uniaxial Compression Based on Advanced Digital Volume Correlation

Haizhou Liu, Lingtao Mao, Xuyang Chang, François Hild

Multiscale damage analyses of red sandstone in uniaxial compression based on advanced digital volume correlation

Haizhou Liu,[1, 2] Lingtao Mao,[1, 3,*] Xuyang Chang,[2] and François Hild[2]

[1] *School of Mechanics and Civil Engineering, China University of Mining & Technology, Beijing 100083, China*
[2]*Université Paris-Saclay, CentraleSupélec, ENS Paris-Saclay, CNRS*
LMPS - Laboratoire de Mécanique Paris-Saclay, 91190 Gif-sur-Yvette, France
[3] *State Key Laboratory of Coal Resources and Safe Mining, China University of Mining & Technology, Beijing 100083, China*
*Corresponding author**:** Lingtao Mao, E-mail: mlt@cumtb.edu.cn

Highlights

- Macroscale, mesoscale, and microscale damage characterization and quantification in uniaxial compression of red sandstone
- Multimesh DVC considering mechanical regularization, damage, and multimesh refinement to measure full-field deformation
- Very fine (sub-voxel) crack opening displacement fields via voxel-scale multimesh DVC to reveal damage initiation and growth

Abstract

X-ray computed tomography (XCT) combined with Digital volume correlation (DVC) has proven to be a powerful tool for bulk deformation measurements of rocks subjected to in-situ experiments. Traditional DVC (*i.e.*, local/global approaches) is generally applied to roughly characterize damage growth by mapping strain localization. However, due to the brittleness of sandstone, damage detection and quantification are very challenging for small spatial resolutions, especially at the microscale (*i.e.,* voxel levels). In this paper, an advanced global approach (*i.e.*, multimesh DVC) was developed, in which mechanical regularization, brittle damage law, and mesh refinement were considered. Such DVC scheme provides an adapted mesh based on damage activity to measure crack opening displacements at the mesoscale and eventually at the voxel-scale. An in-situ uniaxial compression test applied to red sandstone was carried out. Kinematic fields and damage development were analyzed at different scales via multimesh DVC. Macroscale (*i.e.*, specimen-scale) analyses showed the overall deformation characteristics of the specimen by mean strain curves. Mesoscale (*i.e.*, element-scale) results displayed the crack opening displacement fields at sub-voxel resolution. Microscale (*i.e.*, voxel-scale) studies focused on local damage growth using extremely small spatial resolutions (*i.e.*, one voxel). All these investigations quantitatively revealed microcrack initiation, propagation, and coalescence to form the final macrocrack, providing a powerful proof for understanding damage mechanisms in rocks.

Keywords: Digital volume correlation, sandstone, X-ray computed tomography, damage initiation and growth, voxel-scale

Declarations

Funding

This work was financially supported by the National Key Research and Development Program of China (2022YFC2904102), Science Fund for Creative Research Groups of the National Natural Science Foundation of China (52121003), Fundamental Research Funds for the Central Universities of China (2022YJSMT04), and the China Scholarship Council.

Conflicts of interest

The authors declare no conflict of interest.

Availability of data and material

The raw/processed data required to reproduce these findings will be available upon request.

Code availability

The code will be available upon request.

Author Contributions

Haizhou Liu: Conceptualization, Methodology, Investigation, and Writing-Original Draft. **Lingtao Mao:** Resources, Formal analysis, Validation, Supervision and Writing-Review; **Xuyang Chang:** Resources and Supervision; **François Hild:** Conceptualization, Formal analysis, Validation, Supervision and Writing-Review.

List of symbols

b: exponent of power-law interpolation

D: damage variable

f: volume in the reference configuration

$\{\mathbf{f}\}$: nodal force vector

g: volume in the deformed configuration

k: weight factor for uncertainty assessment

$[\mathbf{K}]$: stiffness matrix

$[\mathbf{K}_D^e]$: damaged elementary stiffness matrix

ℓ: mesh size

ℓ_{reg}: regularization length

$\boldsymbol{u}$: sought displacement field

v_i: nodal displacement

$\{\boldsymbol{v}\}$: displacement column vector

w: mechanical weight

ρ_{dvc}: dimensionless correlation residual

ρ_{mec}: mechanical residual

ρ_r : correlation residual

S_{COD}: standard deviation of CODs

ϵ_1: maximum principal strain

ϵ_3: minimum principal strain

ϵ_v: volume strain

σ: standard deviation

σ_z: applied force

σ_{COD}^{std}: standard COD uncertainty

σ_{COD}: COD uncertainty

μ_{COD}: mean value of CODs

V_D: damaged volume

V_{COD}: fraction of damaged volume

σ_{u_x}, σ_{u_y}, σ_{u_z}: standard uncertainties of nodal displacements

σ_{ϵ_1}, σ_{ϵ_2}, σ_{ϵ_3}: standard uncertainties of element-wise principal strains

Φ_c^2 : $L2$-norm of correlation residual

Φ_m^2 : $L2$-norm of force residual

$\boldsymbol{\Psi}_i^{C8}$: shape function of C8 elements

Abbreviations

AE: Acoustic emission

COD: crack opening displacement

DVC: digital volume correlation

FE: Finite element

FWHM: full width at half maximum

GLR: Gray level residual

PMMA: polymethyl methacrylate

ROI: region of interest

RMS: root mean square

VOI: volume of interest

μXCT: X-ray computed microtomography

1. Introduction

Sandstone is a complex geotechnical engineering material featuring naturally occurring damage. It contains cracks and pores, which, in turn, may store gas or water (Liu et al., 2020). Mechanical failure of sandstone is often accompanied by strain localization, which intrinsically is a multiscale spatiotemporal accumulation

process of damage (*i.e.*, crack initiation, propagation, coalescence leading to macroscopic brittle failure (Paterson et al., 2005)). In addition, growing fracture networks may alter the mechanical properties of sandstone when approaching failure (Faulkner et al., 2006). Conventional laboratory tests such as uniaxial (Bagde et al., 2005) and triaxial compression (Yang et al., 2012) combined with Acoustic emission (AE) (Yang et al., 2014; Jia et al., 2020) monitoring have been developed to investigate the strength, deformation behavior and failure characteristics of sandstone at the macroscopic scale. However, the correspondence between microstructure and damage growth cannot be observed in detail. Therefore, it is also desirable to investigate the mechanical response on smaller scales (*e.g.*, micro-or mesoscales).

Numerous measurement techniques have been developed for the evaluation of rock deformation, such as the casting method (Raven et al., 1985), and surface topography measurements (Pyrak-Nolte et al., 2000). The growing use of digital cameras and correlation algorithms offered new ways to measure rock deformation, in which 2D/3D digital image correlation (DIC) techniques are developed to quantify non-destructively the deformation and localization of fracture on the 2D/3D surfaces of rock samples (Zhang et al., 2012; Fakhimi et al., 2018; Xing et al., 2018). Electronic speckle pattern interferometry (ESPI) has also been proved useful to estimate rock deformation (Haggerty et al., 2010). With the development of experimental techniques, X-ray computed microtomography (XCT) has emerged as one promising tool for observing rock microstructures. The early applications were mainly geared toward extracting relevant statistics on different components (*e.g.*, holes, cracks and high-density minerals) before and after testing (Kawakata et al., 1997), including volume fraction, spatial distribution and microstructural features to establish the relationships between structural changes and physical parameters (Ramandi et al., 2016; Moscariello et al., 2018). At this stage, the image resolution was usually small (*e.g.*, tens of micrometers) while the sample size was large. Rock deformation characteristics were described simply and directly, which was based on image processing (*e.g.*, image segmentation and statistics). With the improvement of spatial resolution, micro-focus XCT (*i.e.*, μXCT) gives deeper insight into internal microstructures of rocks down to micro- or even nanoscales (Zhao et al., 2020). Damage development in rocks was further characterized by combining in-situ tests. Renard et al. (2017) reported quantitative and high-resolution internal damage growth in sandstone undergoing brittle failure in triaxial compression. Huang et al. (2019) demonstrated that synchrotron μXCT could be used to directly image in 4 dimensions (3D in space plus time) to analyze the spatiotemporal growth of local porosity and damage at multiple scales in limestone deformed in triaxial compression. In addition, numerical modeling (*e.g.*, pore network modeling method) based on 3D μXCT images is also an attractive way to predict the mechanical properties of sandstone (Vajdova et al. 2004; Han et al. 2014).

For internal deformation field measurement of rocks, digital volume correlation (DVC) has proven to be effective when combined with in-situ/ex-situ tests (Buljac et al., 2018), especially for the evaluation of mesoscopic and macroscopic strain fields at submillimeter resolution. DVC aims to measure displacement fields by registering reference and deformed volumes (Bay et al., 1999). According to the size of the analyzed volume, DVC is divided into local approaches (Smith et al., 2002) (*i.e.*, subsets independently registered) and global approaches (Roux et al., 2008; Hild et al., 2011) (*i.e.*, registration over the *whole* region of interest (ROI) based on finite element discretization). Regularized DVC was further developed to suppress spurious high frequency

components contained in measured displacement fields by adding penalty terms (such as Tikhonov regularization (Bell 1978), curvature penalization (Van Dijk et al., 2019), and mechanical regularization (Leclerc et al., 2011; Mendoza et al., 2019)). These two approaches have been applied to study strain concentrations preceding macroscopic failure of sandstone. Tudisco et al. (2015, 2017) determined 3D strain fields of sandstone during triaxial experiments using local DVC based on neutron tomography and XCT. Their results clearly demonstrated strain localization in the cracked zones. Stappen et al. (2022) used the same algorithm to visualize grain-scale deformation mechanisms of sandstone in triaxial compression with 4D μXCT images. Mao et al. (2020, 2021) investigated the onset and development of strain localization in red sandstone using so-called digital volumetric speckle photography (*i.e.*, local DVC) in different experiments such as indentation and uniaxial compression. Liu et al. (2022) analyzed the localization of normal and shear strains of red sandstone subjected to Brazilian test preceding macroscopic failure using local DVC with adaptive subset sizes, thereby revealing progressive damage accumulation. Renard et al. (2019) presented incremental strain concentrations and fracture coalescence in sandstone subjected to triaxial compression by using image segmentation and local DVC to reveal damage growth at microscopic and macroscopic scales. Hu et al. (2022) performed a uniaxial compression test with a reservoir sandstone and analyzed the gradual change of axial strains by using global DVC. Despite these successful DVC applications on sandstone to characterize damage growth, damage quantifications remained limited especially for microcrack propagation at very small scales (*i.e.*, sub-voxel resolutions). The main challenge comes from the measurement of very rapid fluctuations of displacement fields combined with small-scale spatial resolutions since the limited available information will give rise to high measurement uncertainties (Leclerc et al., 2012). In addition, no damage description was considered in DVC analyses to capture crack opening displacements.

In this work, a multiscale damage analysis of red sandstone has been carried out using in-situ testing and advanced (*i.e.*, multimesh) DVC. The goal is to illustrate the potential of this new DVC approach in contributing to a better understanding of damage development in sandstone from sub-voxel to super-voxel levels. The addressed questions include: when and where do microcracks initiate? How do these microcracks propagate and coalesce with increased loading? What is the proportion and displacement amplitude of microcrack openings preceding failure? The outline of the paper is as follows. In Section 2, uniaxial compression, μXCT system, and red sandstone characteristics are described. In Section 3, the principle of FE-based global DVC is first introduced, then the implementation of multimesh DVC with mechanical regularization, damage variable, and

mesh refinement strategy are described. Section 4 first reports the kinematic and damage fields of the sample in its post-failure state, then a back-to-front damage detection strategy is introduced to evaluate damage growth in pre-failure states at different scales (i.e., macro-, meso-, and microscales).

2. In situ uniaxial compression test

An in-situ uniaxial compression test was performed in a lab tomograph to analyze the damage mechanisms in sandstone**.** The cylinder (25 mm in diameter and 45 mm in height) made of red sandstone used herein was extracted from Jiang Xi Province, China. The sample mainly contained quartz (61 vol%), feldspar (31 vol%) and clay minerals (8 vol%) determined by X-ray diffraction. The main physical and mechanical properties were as follows: density of 2.07 g/cm^3, porosity of 15.1 vol%, Young's modulus (E) equal to 3.3 GPa and Poisson's ratio ν = 0.18. The loading setup for in situ uniaxial compression is shown in Figure 1(a), in which the outer ring was made of polymethyl methacrylate (PMMA). The load and displacement of the upper platen were recorded by the load cell (20 $\pm$ 0.002 kN) and grating displacement meter (20 $\pm$ 0.001 mm), respectively. The maximum axial load was 15 kN and the stroke speed 0.18 mm/min.

[Insert Figure 1 here]

The hardware parameters of XCT are gathered in Table 1. Nineteen scans were performed, namely, two scans in the reference configuration for measurement uncertainty analyses, sixteen scans in the deformed configurations preceding failure, and the last scan for post-failure investigations, which was considered to define the crack path as discussed in Section 4. The axial stress/strain curve is plotted in Figure 1(b), where the corresponding axial stresses preceding failure were 0, 4.1, 8.2, 9.2, 10.2, 11.2, 12.2, 13.2, 14.2, 15.3, 16.3, 17.3, 18.3, 19.3, 20.4, 21.4, and 24.0 MPa, respectively. When reaching the peak stress (27.0 MPa), the sample was completely broken. In each scan, the load was maintained for approximately 25 min, a series of 720 radiographs was acquired to reconstruct 3D images of the sample via Feldkamp cone-beam algorithm (Yang et al., 2016). The load drops correspond to small force relaxations during scan acquisitions.

[Insert Table 1 here]

Figure 2(a) shows 3D renderings (by Tomviz (Schwartz et al., 2012) software) of the volume of interest (VOI) of the sample in the reference configuration. The definition is 700 × 700 × 750 vx with a resolution of 46 µm / vx. No significant artifacts and initial defects are observed in the VOI, and the contrast was uniformly distributed except for several bright spots with high gray levels mostly associated with minerals. Figure 2(b) shows the corresponding gray level histogram with the skewness. The dynamic range of the histogram was approximately 4000 GL (3000-7000 GL), which was limited compared to the 16-bit digitization. The skewness is positive, thus indicating that the histogram was not an ideal Gaussian distribution and the overall trend expanded to the right.

[Insert Figure 2 here]

To compute the equivalent speckle size, the normalized autocorrelation (Minguet et al., 2020) was computed by fast Fourier transform for the VOI in the reference configuration. Figure 3(a) shows the normalized autocorrelation of the VOI (zoom about the correlation peak). The speckle sizes (d) were then

determined as the mean full width at half maximum (FWHM) along the three perpendicular directions (Figure 3(b)). Along the *x*- and *y*-directions, they have a similar level (*i.e.*, ≈2.7 vx), but in the *z*-direction, it is slightly lower (*i.e.*, 2.4 vx), which may be related to rock compaction under gravity. Another way to evaluate the speckle quality is through their contrast, namely, the root-mean-square (RMS) gray level gradients (Leclerc et al., 2012). The values in the three directions are 135, 134 and 138 GL / vx, respectively. According to Leclerc et al. (2012), a larger RMS image gradient gives rise to smaller measurement uncertainties. Therefore, the measurement uncertainty along *z* is expected to be slightly lower than that in the other two directions (*i.e.*, $\sigma_z < \sigma_x \cong \sigma_y$).

[Insert Figure 3 here]

For a better understanding about damage features, 3D renderings of the VOI and middle slices along three perpendicular directions in the post-failure configuration are shown in Figure 4. Severe large-scale cracks are observed in the post-failure scan. In particular, a small piece fell off on the right edge of the sample, which is challenging for DVC measurements. It has to be emphasized that no visible cracks appear on the 3D images prior to macroscopic (brittle) failure, which not only points out the rapid damage process but also the challenges of damage detection and quantification.

[Insert Figure 4 here]

3. Multimesh DVC analyses

3. 1 Principle of regularized DVC

Finite element DVC (Roux et al., 2008; Gomes-Perini et al., 2014) was applied to measure displacement fields from volumetric images acquired during the in situ experiment. Considering the gray level conservation between the volume in the reference state f and deformed configuration g, the correlation residual ρ_r reads

$$\rho_r(\boldsymbol{x}, \{\boldsymbol{v}\}) = f(\boldsymbol{x}) - g[\boldsymbol{x} + \boldsymbol{u}(\boldsymbol{x}, \{\boldsymbol{v}\})] \quad (1)$$

where the sought displacement field $\boldsymbol{u}$ is discretized using 8-noded rectangular hexahedra (*i.e.*, C8 elements $\boldsymbol{u}(\boldsymbol{x}) = \sum_i \boldsymbol{\Psi}_i^{C8}(\boldsymbol{x}) v_i$, where $\boldsymbol{\Psi}_i^{C8}$ are the shape functions corresponding to the nodal displacements v_i). The unknowns then become the nodal displacements v_i that are gathered in the column vector $\{\boldsymbol{v}\}$. A Gauss-Newton (Hild et al., 2016) iteration scheme was used to search for the minimum of the *L*2-norm of the global correlation residual (*i.e.*, $\Phi_c^2(\{\boldsymbol{v}\})$) until reaching a convergence criterion written in terms of the norm of corrections to $\{\boldsymbol{v}\}$. In regularized DVC, linear elasticity is considered in an FE sense by introducing a penalty term based on the equilibrium gap (Claire et al., 2004)

$$[\mathbf{K}]\{\boldsymbol{v}\} = \{\mathbf{f}\} \quad (2)$$

where $[\mathbf{K}]$ is the rectangular stiffness matrix restricted to inner nodes and traction-free surfaces, and $\{\mathbf{f}\}$ the nodal force vector that must vanish in the absence of body forces. The *L*2-norm of the force residuals then reads

$$\Phi_m^2(\{\boldsymbol{v}\}) = \{\boldsymbol{v}\}^{\mathbf{T}}[\mathbf{K}]^{\mathbf{T}}[\mathbf{K}]\{\boldsymbol{v}\} \quad (3)$$

Taking into account these two cost functions leads to the minimization of their weighted sum

$$\{\boldsymbol{v_m}\} = \arg\min \sum_{\mathrm{VOI}} [\Phi_c^2(\{\boldsymbol{v}\}) + w\Phi_m^2(\{\boldsymbol{v}\})] \quad (4)$$

The cost functions are made dimensionless by considering a trial displacement field associated with a plane wave of vector κ (Leclerc et al., 2011). The regularization weight then is proportional to the so-called

regularization length ℓ_{reg} raised to the power 4 (Leclerc et al., 2012)

$$w \propto (2\pi|\kappa|\ell_{reg})^4 \quad \textbf{(5)}$$

Within such regularization scheme, there are two characteristic length scales. The first one is associated with the element size ℓ of the mesh, and the second one is ℓ_{reg}. When $\ell_{\mathrm{reg}} < \ell$, the displacement fluctuations (and their corresponding uncertainties) are controlled by the finite element discretization. Conversely, when $\ell_{\mathrm{reg}} \geq \ell$, the displacement fluctuations are required to be mechanically admissible over a domain whose size is proportional to ℓ_{reg}. Thanks to regularized DVC, it was shown that voxel-scale registrations could be performed (Leclerc et al., 2011; 2012).

3. 2 Damage model

The previous mechanical regularization scheme leads to good approximations when linear elasticity is relevant. However, it no longer applies for elements traversed by cracks (Hild et al., 2015). The corresponding mechanical model is then corrected by introducing a damage variable D ranging from 0 to 1 (*i.e.*, $[\mathbf{K}_D^{\mathbf{e}}]=[\mathbf{K}^{\mathbf{e}}](1-D)$, where $[\mathbf{K}^{\mathbf{e}}]$ and $[\mathbf{K}_D^{\mathbf{e}}]$ are the elementary stiffness matrices before and after correction), which reduces the regularization weight by a factor $\sqrt{1-D}$. Ideally, for brittle damage of sandstone, D should be equal to 1 to fully disable the regularization within individual elements. However, due to limited contrast within very small elements, a low regularization weight was still needed to allow for DVC convergence. Therefore, D tends to be close to 1 as much as possible. In the present case, D was greater than 0.95, which not only ensured DVC convergence, but also allowed high displacement gradients to be captured. Damage zones thus need to be identified. Gray level residuals (GLRs) (Hild et al., 2015; Vrgoč et al., 2021) were shown to be an effective indicator, especially for voxel level crack openings.

3. 3 Refinement and damage relocalization

Considering computational efficiency and measurement uncertainty, a coarse mesh (see cyan mesh in Figure 5) was first used to obtain a rough damage identification. To capture finer damage zones (*i.e.*, morphology of cracks), refinement of the coarse mesh is desirable (Sciuti et al., 2021), see blue mesh in Figure 5. Then, the damage detection quantity (*i.e.*, GLR) was used again in the fine mesh to obtain better resolved crack paths (see red mesh in Figure 5).

[Insert Figure 5 here]

3. 4 Multimesh regularized DVC with damage

Once the above analyses were completed, multimesh and regularized DVC with damage was run. A Master-Slave elimination method (Liu et al., 2013) was used to deal with hanging nodes, which are defined as nodes with different numbers of connectives located on a surface between two elements (black triangle in Figure 5).

The flowchart of the advanced DVC analysis is shown in Figure 6, which includes three steps:

Step 1-global analyses: regularized DVC (coarse mesh) is performed and a damage variable (D) associated with GLR-based damage detection is considered.

Step 2-local analyses: mesh refinement and damage relocalization are carried out for each damaged element.

Step 3-global analyses: multimesh DVC combined with damage is finally run to analyze deformation fields in the presence of cracks.

[Insert Figure 6 here]

4. DVC results and discussion

4. 1 Regularized DVC

4.1.1 Measurement uncertainty

The standard displacement and strain uncertainties were estimated based on two scans in the reference configuration (*i.e.*, scans ref and #0, see Figure 1(b)), which is assessed as the standard deviation σ of the nodal displacements (*i.e.*, σ_{u_x}, σ_{u_y}, σ_{u_z}) and principal strains (*i.e.*, σ_{ϵ_1}, σ_{ϵ_2}, σ_{ϵ_3}) measured by regularized DVC with a mesh size ℓ of 21 voxels (Figure 7(a,b)).

[Insert Figure 7 here]

Similar trends are observed for the fitted power laws ($\sigma \propto \ell_{reg}^{b}$), namely, the larger the regularization length, the lower the standard displacement and strain uncertainties (Leclerc et al., 2012). This general trend was expected because larger regularization lengths correspond to higher mechanical regularization weights, thereby filtering out more high frequency components in deformation fields. The power law exponents of σ_u and σ_ϵ are approximately −1.7 and −2.2, respectively, which are close to theoretical predictions (*i.e.*, $b = -3/2$ for σ_u and $b = -5/2$ for σ_ϵ) (Leclerc et al., 2011). It is worth emphasizing that too large regularization lengths may give rise to excessive boundary effects (Leclerc et al., 2012). In addition, the uncertainty level along the z-direction is smaller than the other two due to better contrast, which is consistent with analyses in terms of RMS gray level gradients. The difference for the three principal strains shows that the maximum (or minimum) principal strains are always more fragile, thus have higher uncertainties.

4.1.2 Registration quality

Two residuals are utilized to evaluate the quality of image registration and mechanical equilibrium, namely, the dimensionless correlation residual ρ_{dvc} and mechanical residual ρ_{mec}

$$\rho_{dvc} = \frac{1}{\max f - \min f}\sqrt{\frac{1}{|\Omega|}\sum_{\boldsymbol{x}}(f(\boldsymbol{x}) - g[\boldsymbol{x}+\boldsymbol{v}(\boldsymbol{x})])^2} \tag{5}$$

$$\rho_{mec} = \sqrt{\{\boldsymbol{v}\}^{\mathrm{T}}[\mathbf{K}]^{\mathrm{T}}[\mathbf{K}]\{\boldsymbol{v}\}} \tag{6}$$

Figure 8 shows the changes of these two residuals for different pre-failure states (except the post-failure state for which the 'relaxation' process stopped at ℓ_{reg}= 60 vx due to severe damage). Similar trends are observed from these results, namely, (1) an increase of ℓ_{reg} reduced ρ_{mec} because more weight is put on mechanical regularization, thus the kinematic description is more constrained leading to larger ρ_{dvc}; (2) both residuals increase with the axial stress for the same regularization length ℓ_{reg} especially when $\ell_{reg} > 60$ vx. Because the linear elastic assumption is gradually less satisfied by the true complex deformation process, the registration quality decreases accordingly; (3) a distinct inflection point is observed for each applied stress, whose regularization length (*i.e.*, $\ell_{reg} = 60$ vx) is considered a suitable choice to balance the two residuals. For lower regularization lengths, the DVC residuals are approximately independent of ℓ_{reg}. Conversely, for large regularization lengths, the two residuals have opposite trends (*i.e.*, significant decrease in ρ_{mec} induces a sharp increase of ρ_{dvc}); (4) the curve for an axial stress of 4.1 MPa is essentially vertical, which suggests that the sample underwent almost pure elastic deformations without too much deviation from mechanical admissibility. The residual ρ_{dvc} changes remain very limited. It is worth noting that the deformation of smaller elements is more likely to be linear and elastic (if undamaged). Therefore, a larger mechanical regularization is expected to act effectively as a low-pass filter; $\ell_{reg} = 60$ vx is still used in analyses with refined meshes.

[Insert Figure 8 here]

4.1.3 Coarse mesh

A first coarse mesh (with a mean length ℓ = 21 vx) is considered for regularized DVC according to the sample geometry, as shown in Figure 9(a,b). To help convergence, a 'relaxation' process (Tomičevć et al., 2013) associated with the regularization length (*i.e.*, ℓ_{reg}= 540, 180, 60, 20, 10, 0 vx) is followed in the DVC calculations. The measured *x*-direction displacement field of the last scan before failure with a regularization length of 60 vx is shown in Figure 9(c). The corresponding displacement uncertainty is less than 0.01 vx (or 0.28 μm) according to the uncertainty analysis of Section 4.1.1 (Figure7(a)). A displacement amplitude of about $\pm$50 μm (or 1.1 vx) occurs in the symmetrical edge region, which illustrates that the deformation before failure is very limited, and damage detection is challenging in the current deformed state.

[Insert Figure 9 here]

4.2 Damage identification in post-failure state

4.2.1 Gray level residuals in coarse mesh

Given the fact that no visible cracks are seen in the pre-failure scans, the crack path is determined with the post-failure scan in which cracks fully developed. Figure 10(a) shows the voxel-wise gray level residual field measured by regularized DVC ($\ell = 21$ vx and $\ell_{reg} = 60$ vx). Figure 10(b) displays the corresponding histogram with two peaks. It also shows the gray level residuals in the *xOy* middle slice (z = 16 mm), which is divided into three smaller regions of interest (*i.e.*, ROI #1, ROI #2 and ROI #3) separated by cracks. A ternary operation is performed on the same slice based on thresholding (*i.e.*, GLR <350 $\rightarrow$ 0, 350≤GLR <850 $\rightarrow$ 1, GLR ≥850 $\rightarrow$ 2, Figure 10(c)). The trinary slice clearly reveals the registration quality of regularized DVC. First, the highest gray level residuals label cracks and highlight where the DVC registration failed. Second, the registration in ROI #1 is deemed trustworthy because it has the lowest gray level residuals except for regions near cracks (due to regularization). On the contrary, higher gray level residuals are observed in ROIs #2 and #3, where untrustworthy registrations occur. It is worth noting that the chip (*i.e.*, right of the blue dotted line) was removed in the subsequent DVC calculations because no grayscale information was available.

[Insert Figure 10 here]

4.2.2 Segmented DVC in coarse mesh

A segmented DVC strategy is considered to deal with the registrations of ROIs #2 and #3. Figure 11(a) shows the gray level residuals in the *xOy* middle slice with laid over mesh nodes in the two regions measured by individual regularized DVC ($\ell = 21$ vx and $\ell_{reg} = 60$ vx). It is to be emphasized that no coarser cracks are contained in the two regions. Low level gray level residuals are observed in these two regions, which proves that the DVC calculations are trustworthy. The nodal displacements in the three ROIs are then merged as initial guess to run regularized DVC ($\ell = 21$ vx and $\ell_{reg} = 60$ vx) for the whole ROI. According to the crack detection procedure (Figure 10(b)), a damage variable (D = 0.98) is selected to capture the presence of cracks. The new gray level residuals for the same slice and the corresponding trinary image are displayed in Figure 11(b,c). Compared to Figure 10(b,c), the gray level residuals in these three regions are reduced except for the cracked regions. In particular, cracks are further recovered and more damage details appear (*e.g.,* two cracks inside the white ellipse in Figure 11(b) while only one is present in Figure 10(b)). The element-wise crack opening displacement (COD) field (see Figure 11(d)) is then evaluated based on the mesh size and the

maximum principal strain (*i.e.*, $\mathrm{COD} \approx \epsilon_1 \ell$). The quantified mean crack opening is approximately 900 μm (or 19.6 vx). However, only a rough match is observed between the crack opening displacement field and gray level residual field due to limitations of the coarse mesh.

[Insert Figure 11 here]

4.2.3 Gray level residual with fine mesh

The detected damaged elements with the coarse mesh are further refined to 5 vx elements, and local regularized DVC is performed to obtain a finer damage localization and initial nodal displacements. Figure 12(a) shows the histogram of gray level residuals for the fine mesh, and the thresholding method (*i.e.*, threshold = 1300 GL) is utilized to detect new damaged elements (Figure 12(b)). The threshold used here is higher than that used in the coarse mesh (*i.e.*, threshold = 850 GL) due to significant crack openings in the fine mesh.

[Insert Figure 12 here]

4.3 Multimesh DVC Analysis

4.3.1 Construction of multimesh

The new finite element table of connectivity is generated according to the mesh information (*i.e.*, coarse mesh, fine mesh, and damage mesh) for multimesh DVC calculations ($\ell_1 = 21$ vx, $\ell_2 = 5$ vx and $\ell_{reg} = 60$ vx, $D = 0.96$). It is worth noting that the damage variable D cannot be set to 1 due to poor contrast in the fine elements. To reduce the computation cost, a contiguous sub-volume containing the cracked surfaces is considered, in which three types of nodes are observed, namely, master (red) nodes in the coarse mesh, slave (blue) nodes, and damaged (green) nodes in the fine mesh (Figure 13). Since damaged nodes are splitable, they should be completely surrounded by slave nodes.

[Insert Figure 13 here]

4.3.2 Crack opening displacement fields

Figure 14 displays different fields characterizing damage (*i.e.*, displacement field in the x-direction, gray level residual field and COD field). Very high displacement gradients (Figure 14(a)) are observed in the cracked regions. Local displacement jumps are greater than 800 μm (or 17.4 vx). The localized zones in the gray level residuals (Figure 14(b)) correspond to the damaged regions. The crack shape is better and finely captured compared to Figure 11(a), which illustrates the benefit of multimesh DVC. The element-wise crack opening displacements (Figure 14(c)) quantify the damaged zones. The total opening in cracked regions is estimated

according to the sum of COD of adjacent damaged elements. For example, the total COD (*i.e.*, 900 μm or 19.6 vx) for the coarse crack in Figure 14(c) corresponds to approximately 3 damaged elements with mean COD of 300 μm.

[Insert Figure 14 here]

4.4 Multiscale damage analyses before failure

Three different characteristic scales are distinguished to describe the details of damage growth in red sandstone under uniaxial compression. At the macroscale, the ROI approaches the entire specimen with a volume of tens of cm^3, and mean strains are used to evaluate the overall damage process. At the mesoscale, the ROI is based on the FE-mesh with a volume scale of tens of mm^3, and element-wise strains are estimated from crack opening displacement fields are deduced. At the microscale, the spatial resolution is generally close to the voxel-scale (*i.e.*, of the order of 50 μm). Therefore, very detailed deformations of the considered body are available.

4.4.1 Macroscale study

Macroscale damage is estimated with the mean strains (*i.e.*, maximum principal strain ϵ_1, minimum principal strain ϵ_3, volumetric strain ϵ_v) over the whole ROI of size $32.2 \times 32.2 \times 34.5$ mm^3 (or $700 \times 700 \times 751$ vx), in which the volumetric strain is defined as the sum of the three principal strains[1]. Figure 15 displays the three mean strains measured by regularized DVC ($\ell = 21$ vx and $\ell_{reg} = 60$ vx) as functions of the applied stress σ_z. The volumetric strain reveals a similar trend with conventional results (Závacký, et al., 2021) and four deformation stages are distinguished. In stage 1 ($0 < \sigma_z < 16.3$ MPa), ϵ_v decreases as σ_z increases, which demonstrates the sample was gradually compressed and ϵ_v is mainly controlled by the minimum (*i.e.,* negative) principal strain ϵ_3. The two principal strain curves approximately exhibit a linear trend, which indicates that no extensive damage occurred in the sample. For stage 2 (16.3 MPa $< \sigma_z < 20.4$ MPa), ϵ_v gradually increases but still remains negative and the two principal strain curves continue to grow but with a nonlinear trend. Such trend indicates the presence of microcracks inside the sample, and ϵ_1 contributes more to ϵ_v. In stage 3 (20.4 MPa $< \sigma_z < 24.0$ MPa), ϵ_v becomes positive, which illustrates the growth of microcracks that leads to volume expansion (*i.e.*, dilatancy) of the sample. Nonlinear trends are observed for the two

[1]The following convention is used. Positive strains refer to expansion, and negative strains to contraction.

principal strain responses. Stage 4 corresponds to the post-failure (unloaded) state of the sample for which the maximum principal strains and volumetric strain experience large increments due to the development of large macrocracks.

[Insert Figure 15 here]

4.4.2 Mesoscale analysis

Mesoscale damage is related to element-wise (*i.e.*, 0.23 mm in the fine mesh) crack opening displacement fields measured by multimesh DVC with the same settings as those used in the post-failure state (Figure 13). There are two reasons for using the post-failure state to assess the damage state. First, it is very difficult to detect microcracks in pre-failure stages especially for small spatial resolutions due to the brittleness of rocks. Therefore, back-to-front damage detection in time sequence can accurately characterizes the initiation and propagation of microcracks. Second, crack openings are expected to be monotonic with increasing loading. Therefore, the complete crack path can be provided by the post-failure state in which the macrocracks are easily detected as they remained open. Back-to-front damage detection combined with measurement uncertainties enables damage growth to be quantified at earlier stages using small spatial resolutions.

The COD threshold is defined as a factor k times the standard COD uncertainty (*i.e.*, $\sigma_{COD} = k\sigma_{COD}^{std}$, with $\sigma_{COD}^{std} = 0.03$ vx or 1.4 µm) assessed with the repeated scan of the reference configuration. The entire crack propagation process is revealed by analyzing crack opening displacement fields after thresholding with different COD thresholds (*i.e.*, k = 3, 4, 5, 6, see Figure 16). It has to be emphasized that the total CODs in the cracked regions should be estimated by the sum of CODs of adjacent damaged elements. The larger the COD threshold, the fewer microcracks appear for the same deformed state. In particular, for the last scan before failure, two microcracked surfaces are observed when factor k is less than 5. However, when factor k is greater than 5, only one microcracked surface appears. Given the fact that the beginning of stage 2 (Figure 15) corresponds to the initiation of microcracks, it should not contain too many microcracks. Therefore, k = 5 is selected to assess the COD detection threshold (*i.e.*, $\sigma_{COD} = 0.15$ vx or 7 µm).

[Insert Figure 16 here]

The mean and standard deviation of CODs (*i.e.*, μ_{COD} and S_{COD}), and the damaged volume (V_D) and its volume fraction (V_{COD}) defined as the percentage of damaged volume are gathered in Table 2. When loaded to 17.3 MPa, scattered microcracks initiate at the bottom of the sample with a mean COD equal to 20.8 µm and a

volume faction of 0.22% (which is the beginning of stage 2 shown in Figure 15). These microcracks gradually coalesce and propagate vertically with a mean COD of 24.1 μm and a volume fraction of 6.3% when reaching an axial stress of 20.4 MPa (*i.e.*, end of stage 2, see Figure 15). Beyond this stress level, the microcracks propagate rapidly with a mean COD $\approx$ 28.2 μm and a volume fraction $\approx$ 36.5%. Only one front microcrack is observed but without the rear one, which presumably initiated during final failure.

[Insert Table 2 here]

4.4.3 Microscale analysis

While mesoscale DVC calculations were carried out successfully to evaluate damage growth of the main cracks, the assessment of the fine cracks is not sufficiently detailed. Therefore, it was necessary to run voxel-scale multimesh DVC to analyze microscale damage that is related to voxel-wise (*i.e.*, 1 voxel $\equiv$ 46 μm) GLRs and voxel-wise CODs. According to the post-failure GLR field (Figure 17(a)) assessed in Section 4.2.2, a small ROI of size 120 × 175 × 10 vx (or 5.5 × 8.1 × 0.5 mm^3) containing one fine crack is chosen (Figure 17(b,c)) considering the computational cost.

[Insert Figure 17 here]

Thresholded mesoscale COD fields in this small ROI measured by regularized DVC ($\ell = 5$ vx, $\ell_{reg} = 60$ vx and $D = 0.99$) are shown in Figure 18. Localized zones are observed only in the last three scans but not in previous ones due to the COD uncertainty (0.17 vx or 7.8 μm) and mesh size limitation. In addition, even though the morphology of cracks at the mesoscale is rather fine, it can be further refined via microscale (or voxel-scale) analyses.

[Insert Figure 18 here]

The detailed implementation steps of voxel-scale multimesh DVC are as follows:

Step 1: Reference ROI and corrected deformed ROI in the post-failure state are shown in Figure 19. The displacement field $\mathbf{u}_1$ for the deformed volume correction is measured by regularized DVC ($\ell = 21$ vx, $\ell_{reg} = 60$ vx, $D = 0.98$).

Step 2: A new FE-mesh of size 5 vx is produced on the ROI. Regularized DVC ($\ell = 5$ vx, $\ell_{reg} = 60$ vx, $\mathbf{u}_0 \leftarrow \mathbf{u}_1$) is run with the initial guess $\mathbf{u}_1$ to obtain nodal displacements $\{\mathbf{u}_2\}$ and the corresponding GLR field (*i.e.*, GLR_2) as shown in Figure 19(b).

Step 3: Damage detection is carried out according to GLR_2 (red mesh in Figure 19(c)). Regularized DVC

is rerun with damage ($\ell = 5$ vx, $\ell_{reg} = 60$ vx, $D = 0.99$, $\mathbf{u}_0 \leftarrow \mathbf{u}_2$) to obtain $\mathbf{u}_3$ and GLR_3.

Step 4: A new FE-multimesh is generated on the ROI, namely, 5 vx-mesh for undamaged zone and 1 vx-mesh (Figure 19(d)) for damaged elements. Multimesh nodal displacements $\mathbf{u}_4$ are interpolated based on $\mathbf{u}_3$.

Step 5: Generate reduced FE-multimesh by taking out the 1 vx-elements belonging to any damaged zone. Run voxel-scale multimesh DVC ($\ell_1 = 5$ vx, $\ell_2 = 1$ vx, $\ell_{reg} = 60$ vx, $\mathbf{u}_0 \leftarrow \mathbf{u}_4$) to calculate $\mathbf{u}_5$ and GLR_5. It is observed that this DVC calculation leads to trustworthy results according to low gray level residuals (Figure 19(e)).

Step 6: Grow one layer of 1 vx-elements along both sides of the cropped zone. Rerun voxel-scale multimesh DVC ($\ell_1 = 5$ vx, $\ell_2 = 1$ vx, $\ell_{reg} = 60$ vx, $\mathbf{u}_0 \leftarrow \mathbf{u}_5$) to calculate $\mathbf{u}_6$ and GLR_6 (Figure 19(f)). Low gray level residuals are observed except for several limited regions, which indicates that almost no damage occurred in the considered meshes and the DVC calculations are trustworthy.

Step 7: Continue growing one layer of 1 vx-elements as above and repeat **Step 6** but with the initial guess of $\mathbf{u}_6$ to calculate $\mathbf{u}_7$ and GLR_7 (Figure 19(g)). This new DVC calculation converged after only a few iterations. Higher gray level residuals occur in the added layer, which indicates that it does contain damage. In particular, the cropped region is very fine and close to 1 vx width. Therefore, **Step 7** can be stopped.

Step 8: Full FE-multimesh displacement fields $\mathbf{u}_8$ are interpolated based on $\mathbf{u}_7$, and thus GLR_8 is calculated in which finer damage localization is observed (Figure 19(h)).

Step 9: Damage detection is carried out again according to GLR_8 (red mesh in Figure 19(i)). Multimesh DVC is run with damage ($\ell_1 = 5$ vx, $\ell_2 = 1$ vx, $\ell_{reg} = 60$ vx, $D = 0.99$, $\mathbf{u}_0 \leftarrow \mathbf{u}_8$) to assess the final nodal displacements $\{\mathbf{u}_f\}$ and the corresponding residuals GLR_f.

[Insert Figure 19 here]

The same DVC settings as described in Figure 19(i) are applied to the pre-failure scans to assess damage growth. The COD threshold is equal to 4.6 μm (or 0.1 vx), which is defined as 5 times the standard COD uncertainty. Table 3 lists the results of the corresponding damage quantification. In addition, thresholded COD fields are plotted around the COD curve vs. axial stress (Figure 20). When loaded to 18.3 MPa, a few scattered microcracks initiate with a mean COD of 5.1 μm (or 0.11 vx), which is very close to the detection threshold, and only a damage volume fraction of 2% is reached. Two microcracks (μ_{COD} = 6.0 μm or 0.13 vx, V_{COD} = 14%) are observed when reaching an axial stress of 20.4 MPa. These two microcracks propagate and gradually

coalesce into a unique mesocrack when loaded to 24.0 MPa. At this point, the damage volume fraction is 48% with a mean COD of 7.5 μm (or 0.16 vx). For the post-failure state, the voxel-level cracks with opening of 40.9 μm (or 0.98 vx) appear. The voxel-scale COD fields reveal damage initiation and propagation very clearly.

[Insert Table 3 here]

[Insert Figure 20 here]

5. Conclusion and perspective

In this work, an in situ uniaxial compression test applied to red sandstone was carried out based on μXCT imaging. Mechanically regularized multimesh DVC considering damage was used to evaluate damage growth at three different scales. In particular, voxel-scale multimesh DVC was implemented to study the early stages of damage inception.

From the macroscopic point of view, the overall deformation of the sample was assessed via mean strain curves (*i.e.*, $\epsilon_1, \epsilon_3, \epsilon_v$) measured over the whole ROI. It was shown that damage had set in for an applied stress equal to 61% (*i.e.*, 16.3 MPa) of the ultimate compressive strength. Microcracks gradually developed leading to dilatancy when the applied stress was greater than 76% (*i.e.*,20.4 MPa) of the ultimate strength. For the post-failure state (*i.e.*, beyond the ultimate stress), macroscale damage occurred suddenly in the form of two longitudinal cracks.

The estimation of element-wised crack opening displacements and crack morphology was carried out and gave more insight into damage growth at the mesoscale, especially for sub-voxel crack opening displacements (CODs). Microcracks initiated from the bottom of the sample, then gradually coalesced and propagated vertically. Only one cracked surface located in the front of the sample was observed for the last scan before failure with a mean COD ≈ 28.2 μm and a volume fraction $\approx$ 36.5%.

The analysis of the gray level residuals and COD fields at the microscale by voxel-scale multimesh DVC enabled damage growth to be characterized and quantified in a very fine way. It provided further understanding of the damage chronology. This study thus demonstrates the potential of multimesh DVC for the quantification of damage at very small scales (*i.e.*, down to the voxel scale).

The significance of this study lies in two points. First, only visible cracks (*i.e.*, CODs greater than one voxel) are generally extracted from CT images. Therefore, sub-voxel openings were hard to capture before the peak loading because of the brittleness of sandstone. However, sub-voxel crack initiation and propagation were clearly measured at earlier stages by the proposed DVC procedure, which is very rare for this type of research.

Second, the kinematic and damage fields of sandstone were quantified for a very fine mesh (*i.e.*, at the voxel-scale), which is impossible in conventional DVC calculations with a spatial resolution of tens of voxels at the least.

The limitation of this study stems from two aspects. First, uniaxial compression is not a strictly continuous process because the applied force is maintained for each scan. Therefore, fast damage growth of sandstone cannot be captured. Second, the computational cost and speed of multimesh DVC are too large and slow for the complete ROI once finer discretization (*e.g.*, at the voxel scale) was considered for cracked regions. Given the above limitations, future work will try to design and perform in situ tests with continuous loading and on-the-fly acquisitions. The corresponding measurement technique will need to be further improved (*e.g.* projection-based DVC, Kosin et al., 2023) to measure bulk deformations and damage in rocks.

References

Bagde MN, Petroš V (2005) Fatigue properties of intact sandstone samples subjected to dynamic uniaxial cyclical loading. Int. J. Rock Mech. Min. Sci. 42(2):237-250. https://doi.org/10.1016/j.ijrmms.2004.08.008

Bay BK, Smith TS, Fyhrie DP, Saad M (1999) Digital volume correlation: Three-dimensional strain mapping using x-ray tomography. Exp Mech 39:217-226. https://doi.org/10.1007/BF02323555

Bell JB, Tikhonov AN, Arsenin VY (1978) Solutions of Ill-Posed Problems. Math Comput 32(144):1320-1322. https://doi.org/10.2307/2006360

Buljac A, Jailin C, Mendoza A, Neggers J, Taillandier T, Bouterf A, Smaniotto B, Hild F, Roux S (2018) Digital Volume Correlation: Review of Progress and Challenges. Exp Mech 58:661-708. https://doi.org/10.1007/s11340-018-0390-7

Claire D, Hild F, Roux S (2004) A finite element formulation to identify damage fields: The equilibrium gap method. Int J Numer Methods Eng 61(2):189-208. https://doi.org/10.1002/nme.1057

Van Stappen J, McBeck JA, Cordonnier B, Pijnenburg R, Renard F, Spiers C, Hangx S (2022) 4D Synchrotron X-ray Imaging of Grain Scale Deformation Mechanisms in a Seismogenic Gas Reservoir Sandstone During Axial Compaction. Rock Mech Rock Eng 55:4697–4715. https://doi.org/10.1007/s00603-022-02842-7

Faulkner DR, Mitchell TM, Healy D, Heap MJ (2006) Slip on "weak" faults by the rotation of regional stress in the fracture damage zone. Nature 444:922-925. https://doi.org/10.1038/nature05353

Fakhimi A, Lin Q, Labuz JF (2018) Insights on rock fracture from digital imaging and numerical modeling. Int.

J. Rock Mech. Min. Sci., 107:201-207. https://doi.org/10.1016/j.ijrmms.2018.05.002

Gomes-Perini LA, Passieux JC, Périé JN (2014) A multigrid PGD-based algorithm for volumetric displacement fields measurements. Strain 50(4):355-367. https://doi.org/10.1111/str.12099

Haggerty M, Lin Q, Labuz JF (2010) Observing deformation and fracture of rock with speckle patterns. Rock Mech. Rock Eng. 43(4):417-426. https://doi.org/10.1007/s00603-009-0055-z

Han Y, Hu D, Matzar L (2014) Numerical computation of elastic properties for porous rocks based on CT-scanned images using direct mapping method. J Pet Sci Eng 122:346-353. https://doi.org/10.1016/j.petrol.2014.07.029

Hild F, Bouterf A, Chamoin L, Leclerc H, Mathieu F, Neggers J, Pled F, Tomičević Z, Roux S (2016) Toward 4D mechanical correlation. Adv Model Simul Eng Sci 3(1):1-26. https://doi.org/10.1186/s40323-016-0070-z

Hild F, Bouterf A, Roux S (2015) Damage measurements via DIC. Int J Fract 191:77-105. https://doi.org/10.1007/s10704-015-0004-7

Hild F, Fanget A, Adrien J, Maire E, Roux S (2011) Three-dimensional analysis of a tensile test on a propellant with digital volume correlation. Arch Mech 63(5-6):1-20. https://hal.archives-ouvertes.fr/hal-00634714

Hu C, Jia Y, Duan Z (2022) Pore and permeability properties of reservoir sandstone under a uniaxial compression CT test. J Nat Gas Sci Eng 104:104666. https://doi.org/10.1016/j.jngse.2022.104666

Huang L, Baud P, Cordonnier B, Renard F, Liu L, Wong T (2019) Synchrotron X-ray imaging in 4D: Multiscale failure and compaction localization in triaxially compressed porous limestone. Earth Planet Sci Lett 528:115831. https://doi.org/10.1016/j.epsl.2019.115831

Jia Z, Xie H, Zhang R, Li C, Wang M, Gao M, Zhang Z, Zhang Z (2020) Acoustic Emission Characteristics and Damage Evolution of Coal at Different Depths Under Triaxial Compression. Rock Mech Rock Eng 53:2063-2076. https://doi.org/10.1007/s00603-019-02042-w

Kawakata H, Cho A, Yanagidani T, Shimada M (1997) The observations of faulting in Westerly granite under triaxial compression by X-ray CT scan. Int J Rock Mech Min Sci 34(3-4):151. https://doi.org/10.1016/S1365-1609(97)00138-X

Kosin V, Fau A, Jailin C, Smaniotto B, Wick T, Hild F (2023) A projection-based approach to extend digital volume correlation for 4D spacetime measurements. C R Mécanique, in press. https://doi.org/10.5802/crmeca.192

Leclerc H, Périé JN, Hild F, Roux S (2012) Digital volume correlation: What are the limits to the spatial resolution? Mech Ind 13(6):361-371. https://doi.org/10.1051/meca/2012025

Leclerc H, Périé JN, Roux S, Hild F (2011) Voxel-Scale Digital Volume Correlation. Exp Mech 51(4):479-490. https://doi.org/10.1007/s11340-010-9407-6

Liu GR (2013) The Finite Element Method A Practical Course. Finite Element Method

Liu HZ, Mao L, Ju Y, Chiang FP (2022) An Adaptive and Reliable Guided Digital Volume Correlation Algorithm for Sandstone Based on 3D Scale-Invariant Feature Transform. Rock Mech Rock Eng 55(10):6171–6186. https://doi.org/10.1007/s00603-022-02986-6

Liu HZ, Yang G, Yun Y, Lin J, Ye W, Zhang H, Zhang Y (2020) Investigation of Sandstone Mesostructure Damage Caused by Freeze-Thaw Cycles via CT Image Enhancement Technology. Advances in Civil Engineering 2020. https://doi.org/10.1155/2020/8875814

Mao LT, Liu HZ, Wang YW, Ding LL, Ju Y, Chiang FP (2021) 3-D strain estimation in sandstone using improved digital volumetric speckle photography algorithm. Int J Rock Mech Min Sci 141. https://doi.org/10.1016/j.ijrmms.2021.104736

Mao LT, Zhu Y, Wang YW, Liu YF (2020) An Improved Digital Volumetric Speckle Photography Technique with X-ray Microtomography and its Applications to Investigating Strain Localization in Red Sandstone. Rock Mech Rock Eng 53(3):1457-1466. https://doi.org/10.1007/s00603-019-01971-w

Mendoza A, Neggers J, Hild F, Roux S (2019) Complete mechanical regularization applied to digital image and volume correlation. Comput Methods Appl Mech Eng 355:27-43. https://doi.org/10.1016/j.cma.2019.06.005

Minguet C, Soulas F, Lafargue-Tallet T, Chalumeau E, Pommies M, Peiffer R, Hild F (2020) On the validation of a priori estimates of standard displacement uncertainties in T3-stereocorrelation. Meas Sci Technol 32(2):024004. https://doi.org/10.1088/1361-6501/abafe1

Moscariello M, Cuomo S, Salager S (2018) Capillary collapse of loose pyroclastic unsaturated sands characterized at grain scale. Acta Geotech 13(1):117-133. https://doi.org/10.1007/s11440-017-0603-8

Paterson MS, Wong TF (2005) Experimental rock deformation - The brittle field. Berlin: Springer. https://doi.org/10.1007/b137431

Pyrak-Nolte LJ, Morris JP (2000). Single fractures under normal stress: the relation between fracture specific stiffness and fluid flow, Int J Rock Mech Min Sci 37(1–2):245-262.

https://doi.org/10.1016/S1365-1609(99)00104-5

Raven KG, Gale JE (1985) Water flow in a natural rock fracture as a function of stress and sample size. Int J Rock Mech Min Sci Geomech Abstracts 22(4):251-261. https://doi.org/10.1016/0148-9062(85)92952-3

Ramandi HL, Mostaghimi P, Armstrong RT, Saadatfar M, Pinczewski W (2016) Porosity and permeability characterization of coal: A micro-computed tomography study. Int J Coal Geol 154–155:57-68. https://doi.org/10.1016/j.coal.2015.10.001

Renard F, Cordonnier B, Kobchenko M, Kandula N, Weiss J, Zhu W (2017) Microscale characterization of rupture nucleation unravels precursors to faulting in rocks. Earth Planet Sci Lett 476:69-78. https://doi.org/10.1016/j.epsl.2017.08.002

Renard F, McBeck J, Cordonnier B, Zheng X, Kandula N, Sanchez J, Kobchenko M, Noiriel C, Zhu W, Meakin P, Fusseis F, Dysthe D (2019) Dynamic In Situ Three-Dimensional Imaging and Digital Volume Correlation Analysis to Quantify Strain Localization and Fracture Coalescence in Sandstone. Pure Appl Geophys 176:1083-1115. https://doi.org/10.1007/s00024-018-2003-x

Roux S, Hild F, Viot P, Bernard D (2008) Three-dimensional image correlation from X-ray computed tomography of solid foam. Compos Part A 39(8):1253-1265. https://doi.org/10.1016/j.compositesa.2007.11.011

Schwartz J, Harris C, Pietryga J, Zheng H, Kumar P, Visheratina A, Kotov N, Major B, Avery P, Ercius P, Ayachit U, Geveci B, Muller D, Genova A, Jiang Y, Hanwell M, Hovden R (2022) Real-time 3D analysis during electron tomography using tomviz. Nat Commun 13(1):1-7. https://doi.org/10.1038/s41467-022-32046-0

Sciuti VF, Vargas R, Canto RB, Hild F (2021) Pyramidal adaptive meshing for Digital Image Correlation dealing with cracks. Eng Fract Mech 256:107931. https://doi.org/10.1016/j.engfracmech.2021.107931

Smith TS, Bay BK, Rashid MM (2002) Digital volume correlation including rotational degrees of freedom during minimization. Exp Mech 42:272-278. https://doi.org/10.1177/001448502321548346

Tomičevć Z, Hild F, Roux S (2013) Mechanics-aided digital image correlation. J Strain Anal Eng Des 48(5):330-343. https://doi.org/10.1177/0309324713482457

Tudisco E, Hall SA, Charalampidou EM, Kardjilov N, Hilger A, Sone H (2015) Full-field Measurements of Strain Localisation in Sandstone by Neutron Tomography and 3D-Volumetric Digital Image Correlation. Phys. Procedia 69:509-515. https://doi.org/10.1016/j.phpro.2015.07.072

Tudisco E, Jailin C, Mendoza A, Tengattini A, Andò E, Hall S, Viggiani G, Hild F, Roux S (2017) An extension of digital volume correlation for multimodality image registration. Meas Sci Technol 28(9):095401. https://doi.org/10.1088/1361-6501/aa7b48

Vajdova V, Baud P, Wong TF (2004) Permeability evolution during localized deformation in Bentheim sandstone. J Geophys Res Solid Earth 109(B10). https://doi.org/10.1029/2003JB002942

van Dijk NP, Wu D, Persson C, Isaksson P (2019) A global digital volume correlation algorithm based on higher-order finite elements: Implementation and evaluation. Int J Solids Struct 168:211-227. https://doi.org/10.1016/j.ijsolstr.2019.03.024

Vrgoč A, Tomičević Z, Smaniotto B, Hild F (2021) Damage characterization in fiber reinforced polymer via Digital Volume Correlation. Coupled Syst Mech 10(6):545-560. https://doi.org/10.12989/csm.2021.10.6.545

Xing H.Z. Zhang Q.B, Ruan D, Dehkhoda S, Lu G.X, Zhao J (2018) Full-field measurement and fracture characterisations of rocks under dynamic loads using high-speed three-dimensional digital image correlation. Engineering 113:61-72. https://doi.org/10.1016/j.ijimpeng.2017.11.011

Yang M, Liu J, Li Z, Liang L, Wang X, Gui Z (2016) Locating of 2π-projection view and projection denoising under fast continuous rotation scanning mode of micro-CT. Neurocomputing 207:335-345. https://doi.org/10.1016/j.neucom.2016.05.018

Yang SQ, Jing HW, Wang SY (2012) Experimental investigation on the strength, deformability, failure behavior and acoustic emission locations of red sandstone under triaxial compression. Rock Mech Rock Eng 45:583-606. https://doi.org/10.1007/s00603-011-0208-8

Yang SQ, Ni HM, Wen S (2014) Spatial acoustic emission evolution of red sandstone during multi-stage triaxial deformation. J Cent South Univ 21:3316-3326. https://doi.org/10.1007/s11771-014-2305-9

Závacký M, Štefaňák J (2019) Strains of rock during uniaxial compression test. Civil Eng J 32(3):398-403. https://doi.org/10.14311/CEJ.2019.03.0032

Zhang H, Zhang, G, Huang, H, Song, Y Kang (2012) Experimental investigation of deformation and failure mechanisms in rock under indentation by digital image correlation. Eng. Fract. Mech. 96:667-675. https://doi.org/10.1016/j.engfracmech.2012.09.012

Figure Captions

Fig. 1. In situ setup for uniaxial compression (a) and axial stress/strain curve (b) depicting the 19 scans acquisitions of the in situ test

Fig 2. (a) 3D renderings of the VOI in the reference configuration. (b) Corresponding gray level histogram with skewness

Fig 3. (a) Normalized autocorrelation of the VOI in the reference configuration. (b) Characteristic speckle sizes along three perpendicular directions determined by its FWHM

Fig 4. 3D renderings of the post-failure configuration. (a) VOI. and (b) middle slices (*i.e.*, *xOy* plane for z = 16 mm, *yOz* plane for x = 15.5 mm, *xOz* plane for y = 15.5 mm)

Fig. 5 Example of mesh refinement and damage relocalization

Fig. 6 Flowchart of multimesh DVC analyses in the presence of cracks

Fig 7. Standard displacement (a) and strain (b) uncertainties as functions of regularization length. The solid lines depict power-law interpolation with exponent b

Fig. 8 Mechanical residual ρ_{mec} as a function of dimensionless correlation residual ρ_{dvc} for different applied loads and regularization lengths

Fig. 9 Coarse mesh shown in *xOy* (a) and *xOz* (b) planes for the reference configuration. (c) Measured displacement field (ℓ_{reg}= 60 vx) in the x-direction for the last pre-failure state

Fig. 10 Gray level residual fields in the post-failure state. (a) 3D rendering (values less than 850 GL are transparent). (b) Gray level residuals in the z-direction middle slice (see red dotted circle in subfigure(a)) and its histogram with thresholding values. (c) Trinary image after thresholding

Fig. 11 Segmented DVC results. (a) Segmentation and DVC analyses in two individual regions (*i.e.*, ROIs #2 and #3). (b) Gray level residuals in the z-direction middle slice measured by regularized DVC (D = 0.98). (c) Trinary image after thresholding. (4) Crack opening displacement field in the same slice.

Fig. 12 Damage detection in the fine mesh. (a) Histograms of elementary GLRs and selected threshold. (b) 3D rendering of damaged elements

Fig. 13 Schematic view of nodes in multimesh DVC. (a) 3D rendering. (b) Middle *xOy* slice (z = 15 mm). The red nodes depict masters, blue nodes are slaves, and damaged nodes are green

Fig. 14 Damage related fields measured by multimesh DVC. The top row shows 3D renderings and the bottom row the corresponding middle *xOy* slice. (a) Displacement along x-direction (in μm). (b) Gray level residuals. (c) Crack opening displacement (in μm)

Fig. 15 Mean measured strains as functions of axial stress and the four deformation stages

Fig. 16 Thresholded mesoscale COD fields for different axial stresses and with four different COD thresholds

corresponding to k times the standard COD uncertainty

Fig. 17 Schematic view of gray level residual field. (a) 3D rendering. (b) 10 vx-high volume containing two main cracks and one fine crack. (c) Zoom of the selected small ROI.

Fig. 18 Thresholded mesoscale COD fields for different axial stresses. (a) 21.4 MPa. (b) 24.0 MPa. (c) post-failure

Fig. 19 All voxel-scale multimesh DVC steps. (a) 3D renderings of ROI in the reference (bottom) and corrected deformed (*i.e.*, post-failure) configurations (top). (b) FE-mesh with size of 5 vx (bottom) and normalized GLR field measured by regularized DVC (top). (c) FE-mesh with damage highlighted in red (bottom) and normalized GLR field measured by regularized DVC with damage (top). (d) FE-multimesh containing 5 vx-elements (cyan) and 1 vx-elements (yellow). (e) Reduced FE-multimesh (bottom) and normalized GLR field measured by voxel-scale multimesh DVC (top). (f) Reduced FE-multimesh after adding one layer with 1 vx-elements (bottom) and normalized GLR field measured by voxel-scale multimesh DVC (top). (g) Reduced FE-multimesh after adding two layers of 1 vx-elements (bottom) and normalized GLR field measured by voxel-scale multimesh DVC (top). (h) Normalized GLR field calculated by the full FE-multimesh displacement field. (i) FE-multimesh with damage highlighted in red (bottom) and normalized GLR field (top).

Fig. 20 Thresholded microscale COD fields and corresponding mean COD and its standard deviation (error bars)

Table Captions

Table 1 XCT hardware parameters

Table 2 Damage quantification at the mesoscale

Table 3 Damage quantification at the microscale

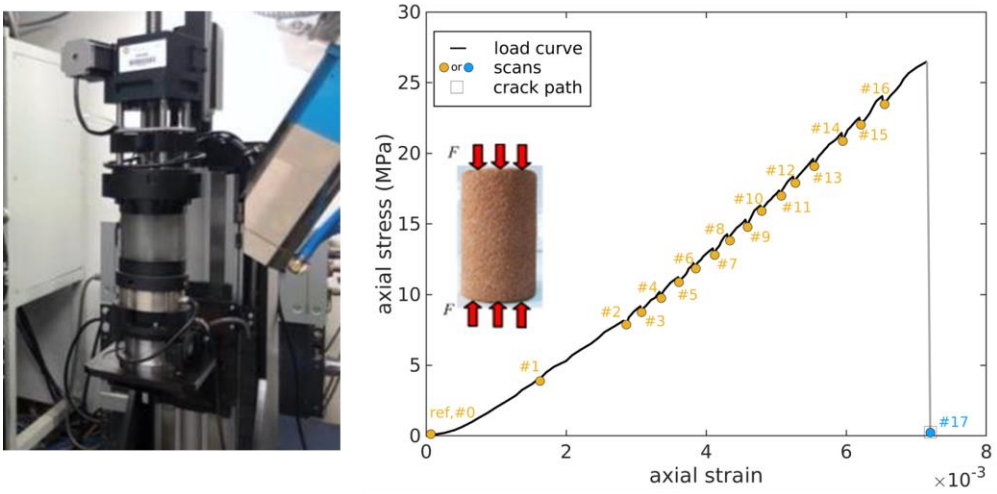
load curve
scans
crack path
F
F
axial stress (MPa)
axial strain
×10-3
ref,#0
#1
#2
#3
#4
#5
#6
#7
#8
#9
#10
#11
#12
#13
#14
#15
#16
#17

(a) (b)

Fig. 1

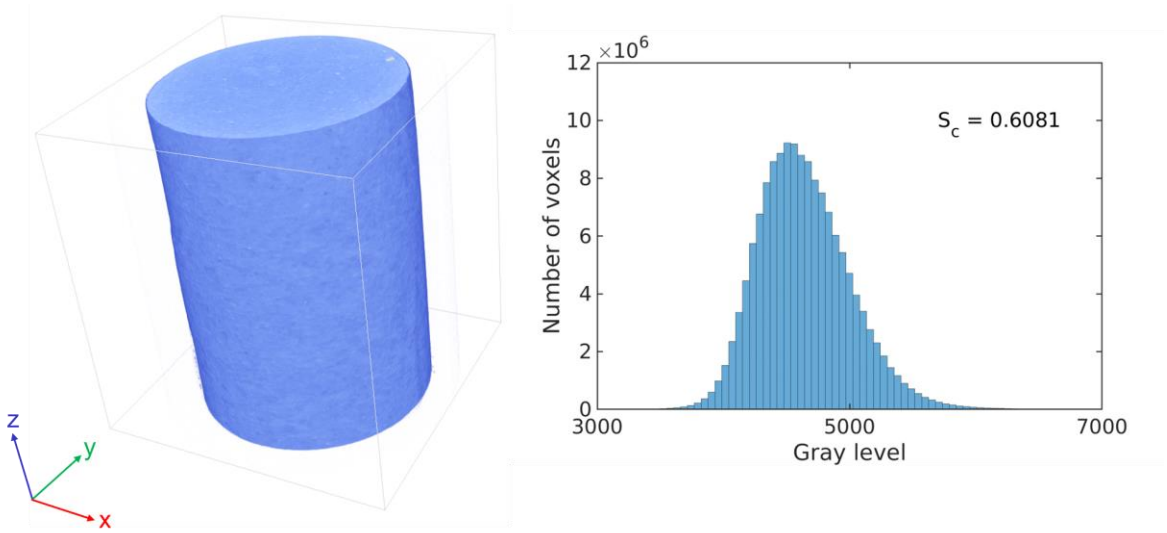
z
y
x
×10^6
12
10
8
6
4
2
0
Number of voxels
S_c = 0.6081
3000
5000
7000
Gray level

(a) (b)

Fig. 2

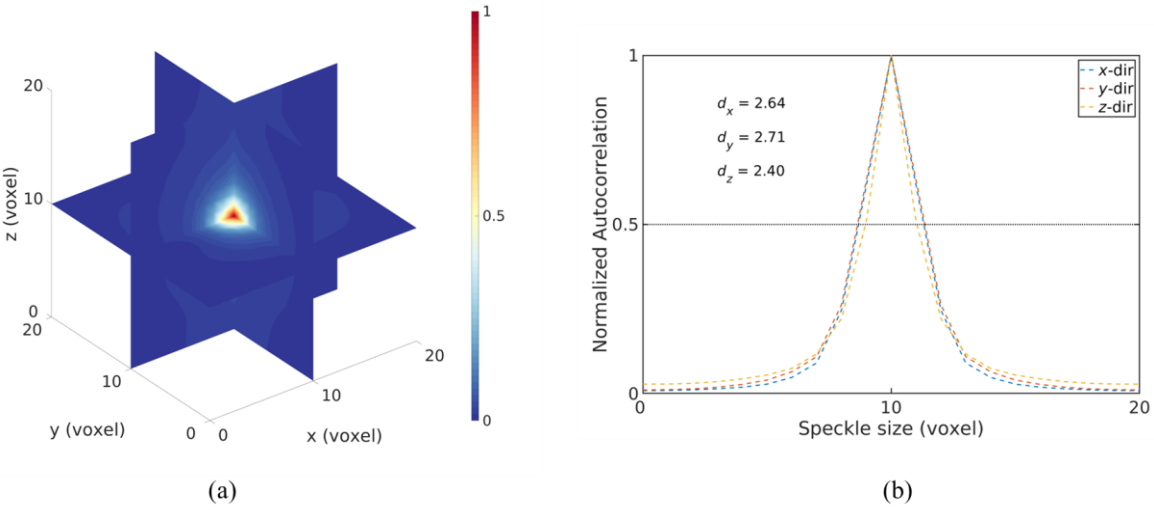
z (voxel)
y (voxel)
x (voxel)
Normalized Autocorrelation
Speckle size (voxel)
d_x = 2.64
d_y = 2.71
d_z = 2.40
x-dir
y-dir
z-dir

(a) (b)

Fig. 3

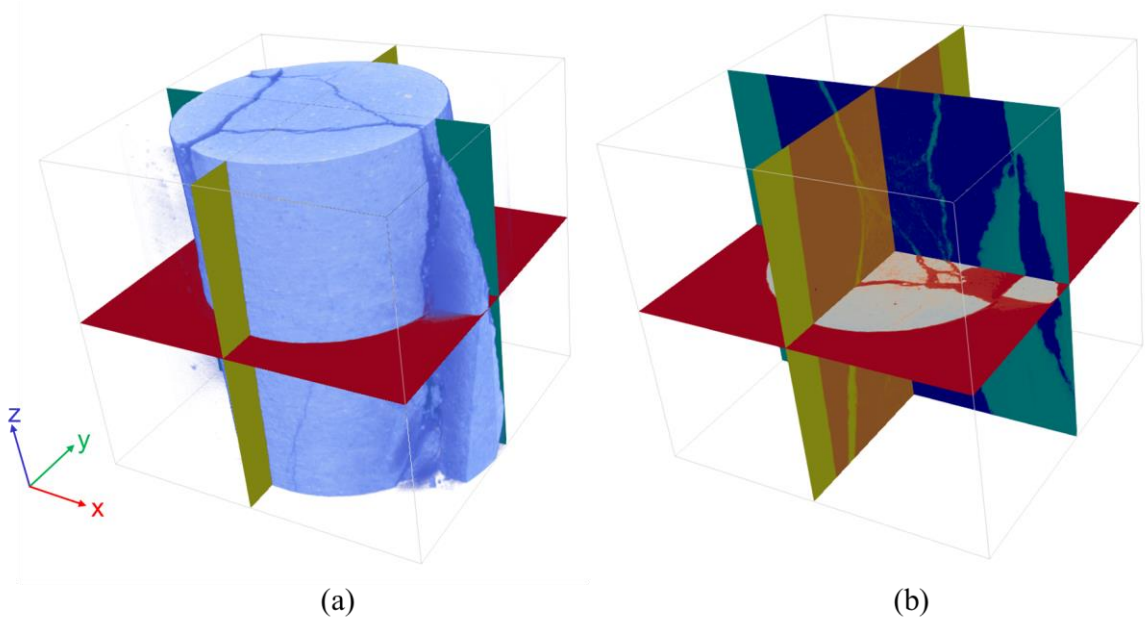

Fig. 4

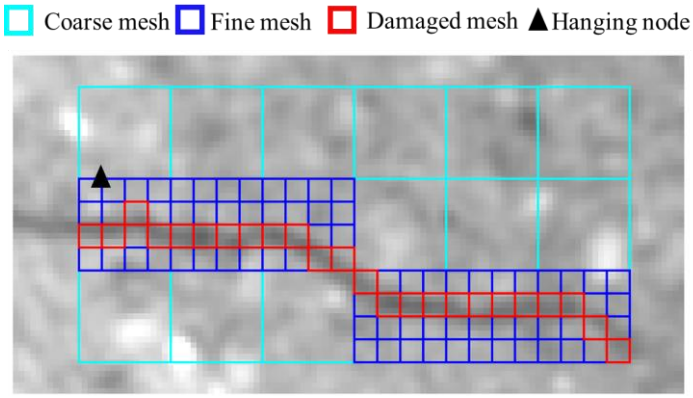

Fig. 5

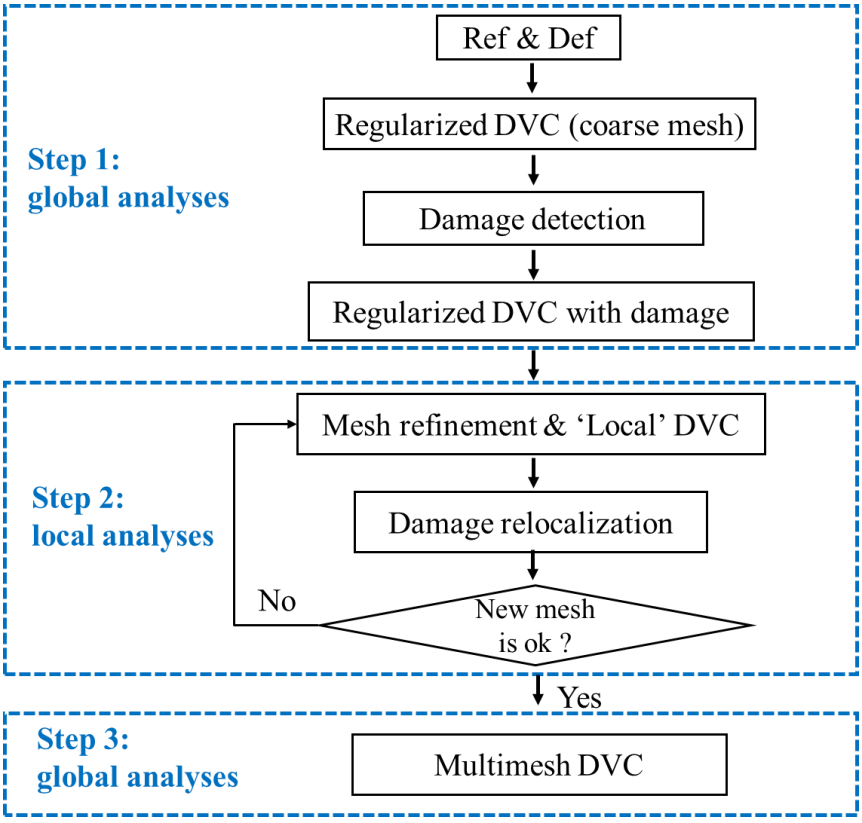
Step 1:
global analyses
Ref & Def
Regularized DVC (coarse mesh)
Damage detection
Regularized DVC with damage
Step 2:
local analyses
Mesh refinement & 'Local' DVC
Damage relocalization
No
New mesh
is ok ?
Yes
Step 3:
global analyses
Multimesh DVC

Fig. 6

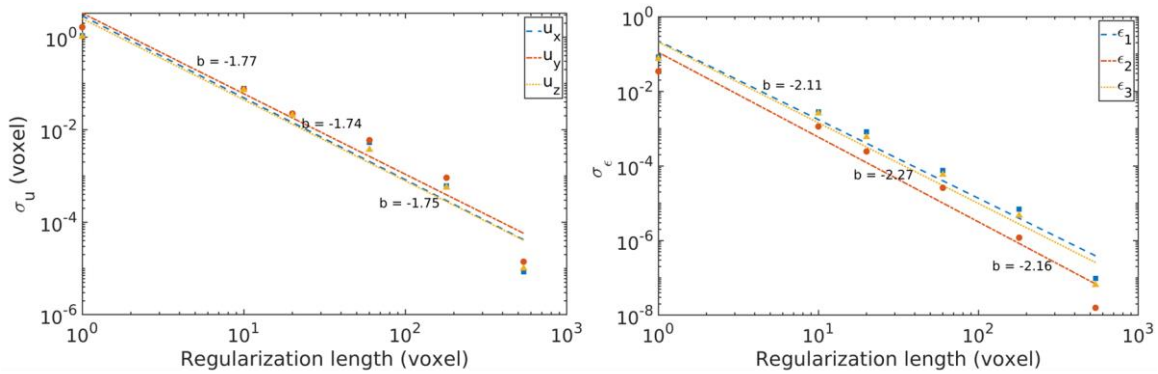
10^0
10^{-2}
10^{-4}
10^{-6}
σ_u (voxel)
b = -1.77
b = -1.74
b = -1.75
u_x
u_y
u_z
10^0
10^1
10^2
10^3
Regularization length (voxel)
10^0
10^{-2}
10^{-4}
10^{-6}
10^{-8}
σ_ϵ
b = -2.11
b = -2.27
b = -2.16
ϵ_1
ϵ_2
ϵ_3
10^0
10^1
10^2
10^3
Regularization length (voxel)

(a) (b)

Fig. 7

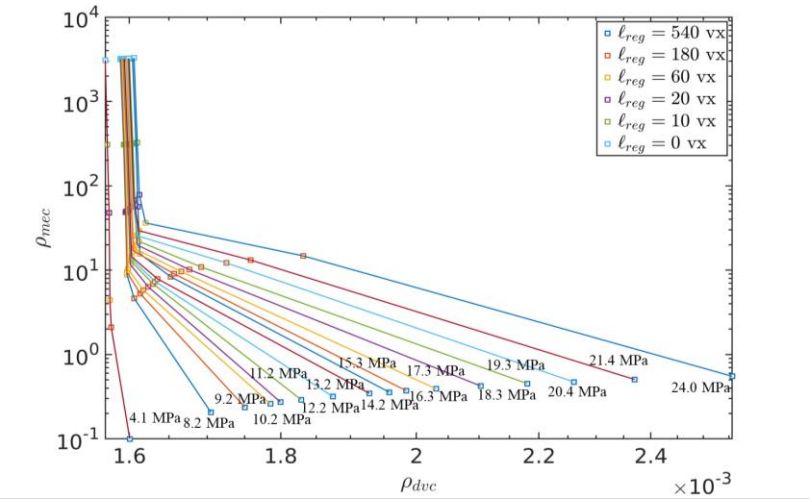
$\ell_{reg} = 540$ vx
$\ell_{reg} = 180$ vx
$\ell_{reg} = 60$ vx
$\ell_{reg} = 20$ vx
$\ell_{reg} = 10$ vx
$\ell_{reg} = 0$ vx
ρ_{mec}
ρ_{dvc}
$\times 10^{-3}$
4.1 MPa
8.2 MPa
9.2 MPa
10.2 MPa
11.2 MPa
12.2 MPa
13.2 MPa
14.2 MPa
15.3 MPa
16.3 MPa
17.3 MPa
18.3 MPa
19.3 MPa
20.4 MPa
21.4 MPa
24.0 MPa

Fig. 8

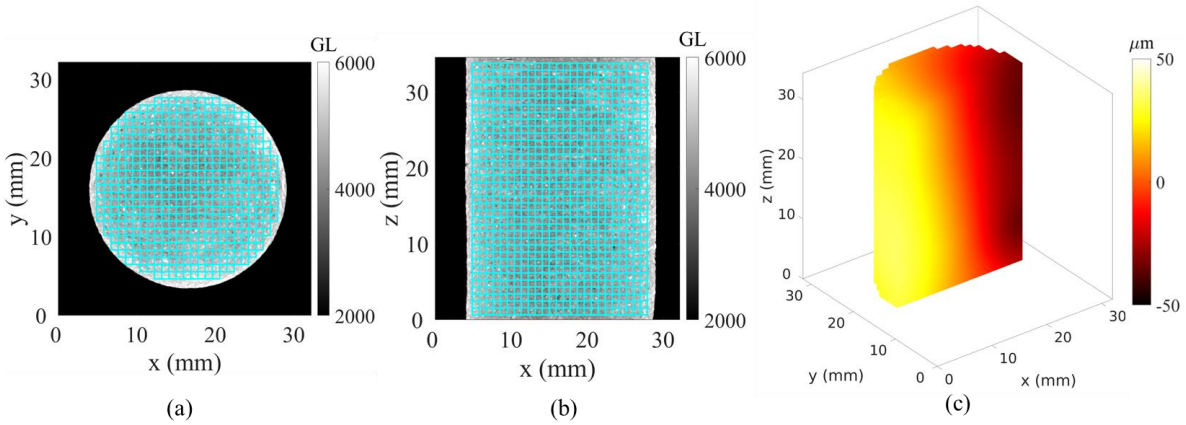
GL
6000
4000
2000
y (mm)
x (mm)
(a)
GL
6000
4000
2000
z (mm)
x (mm)
(b)
μm
50
0
-50
z (mm)
y (mm)
x (mm)
(c)

Fig. 9

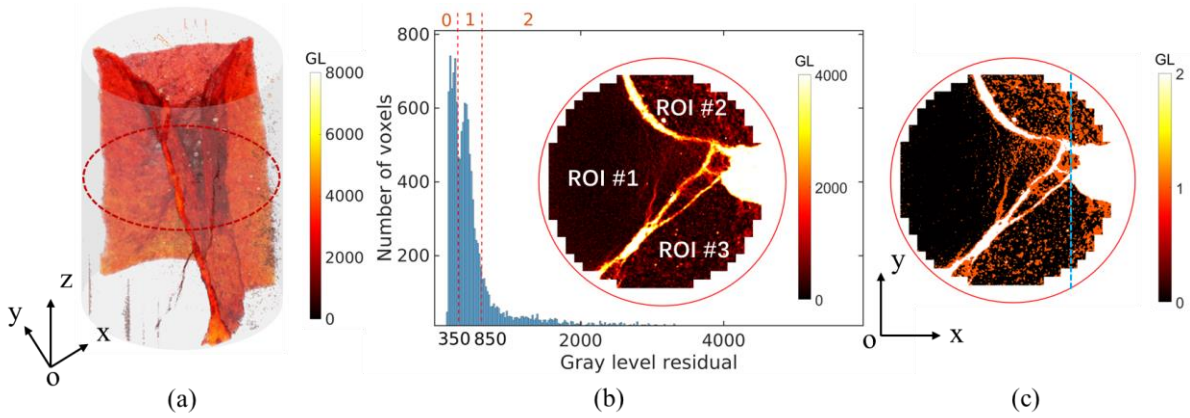
GL
8000
6000
4000
2000
0
z
y
x
o
(a)
0
1
2
800
600
400
200
Number of voxels
350 850
2000
4000
Gray level residual
ROI #1
ROI #2
ROI #3
GL
4000
2000
0
(b)
y
x
o
GL
2
1
0
(c)

Fig. 10

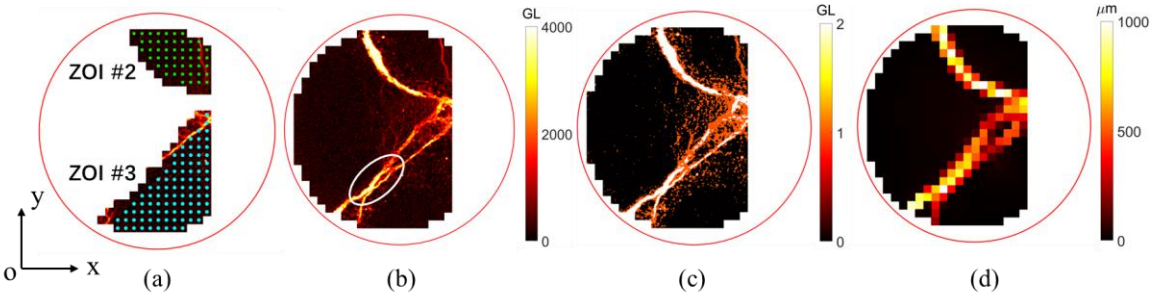

Fig. 11

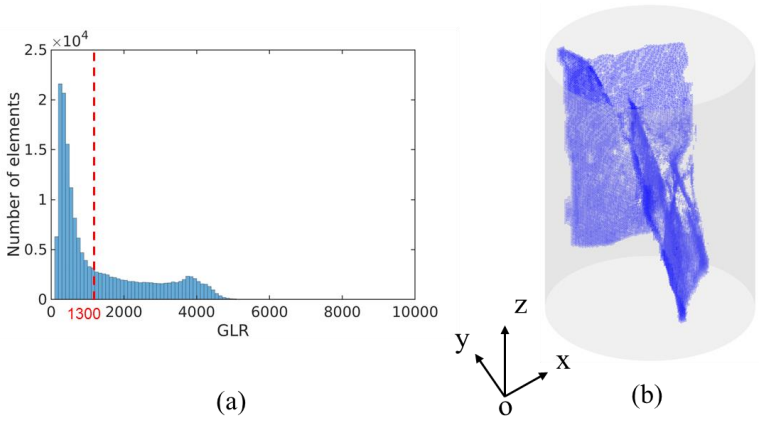
×10^4
2.5
2
1.5
1
0.5
0
Number of elements
0
1300
2000
4000
6000
8000
10000
GLR
(a)
z
y
x
o
(b)

Fig. 12

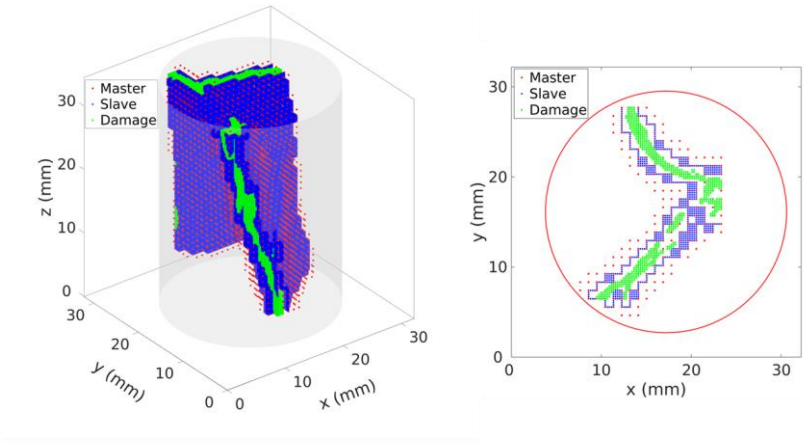

(a) (b)

Fig. 13

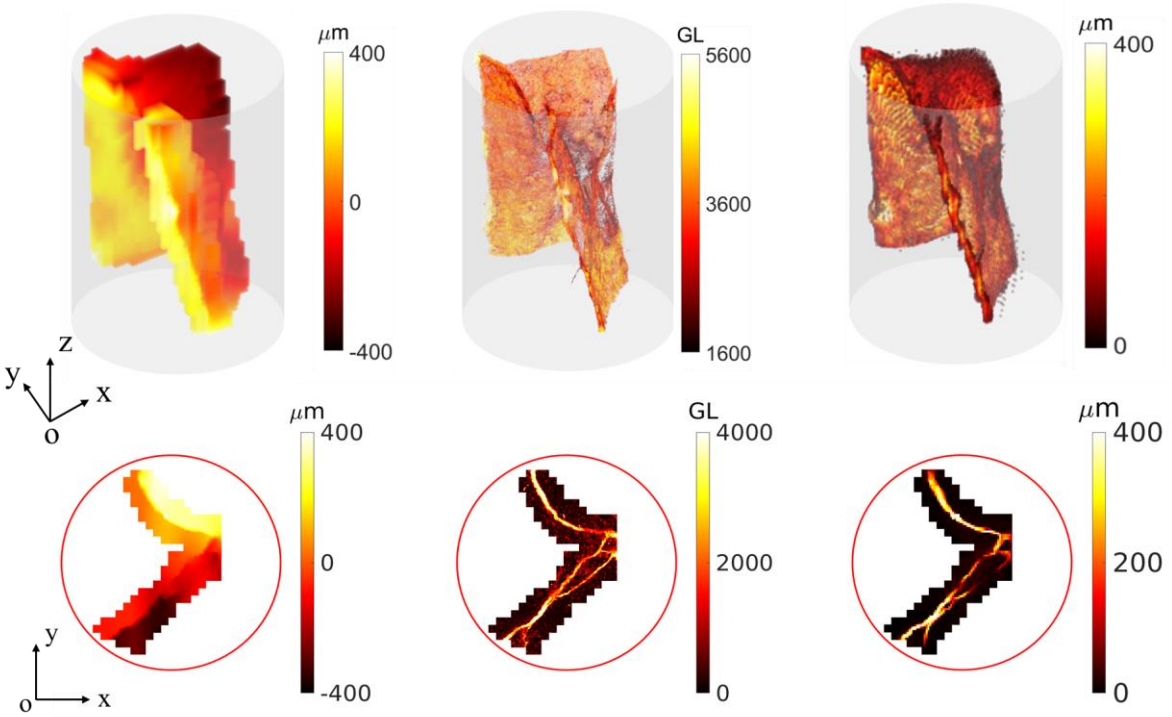
μm
400
0
-400
GL
5600
3600
1600
μm
400
0
z
y
x
o
μm
400
0
-400
GL
4000
2000
0
μm
400
200
0
y
x
o
(a)
(b)
(c)

Fig. 14

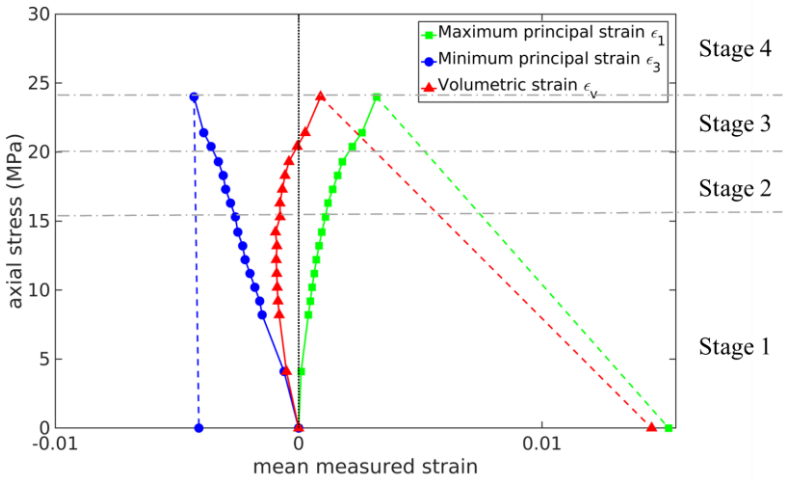
Maximum principal strain ϵ_1
Minimum principal strain ϵ_3
Volumetric strain ϵ_v
Stage 4
Stage 3
Stage 2
Stage 1
axial stress (MPa)
mean measured strain
30
25
20
15
10
5
0
-0.01
0
0.01

Fig. 15

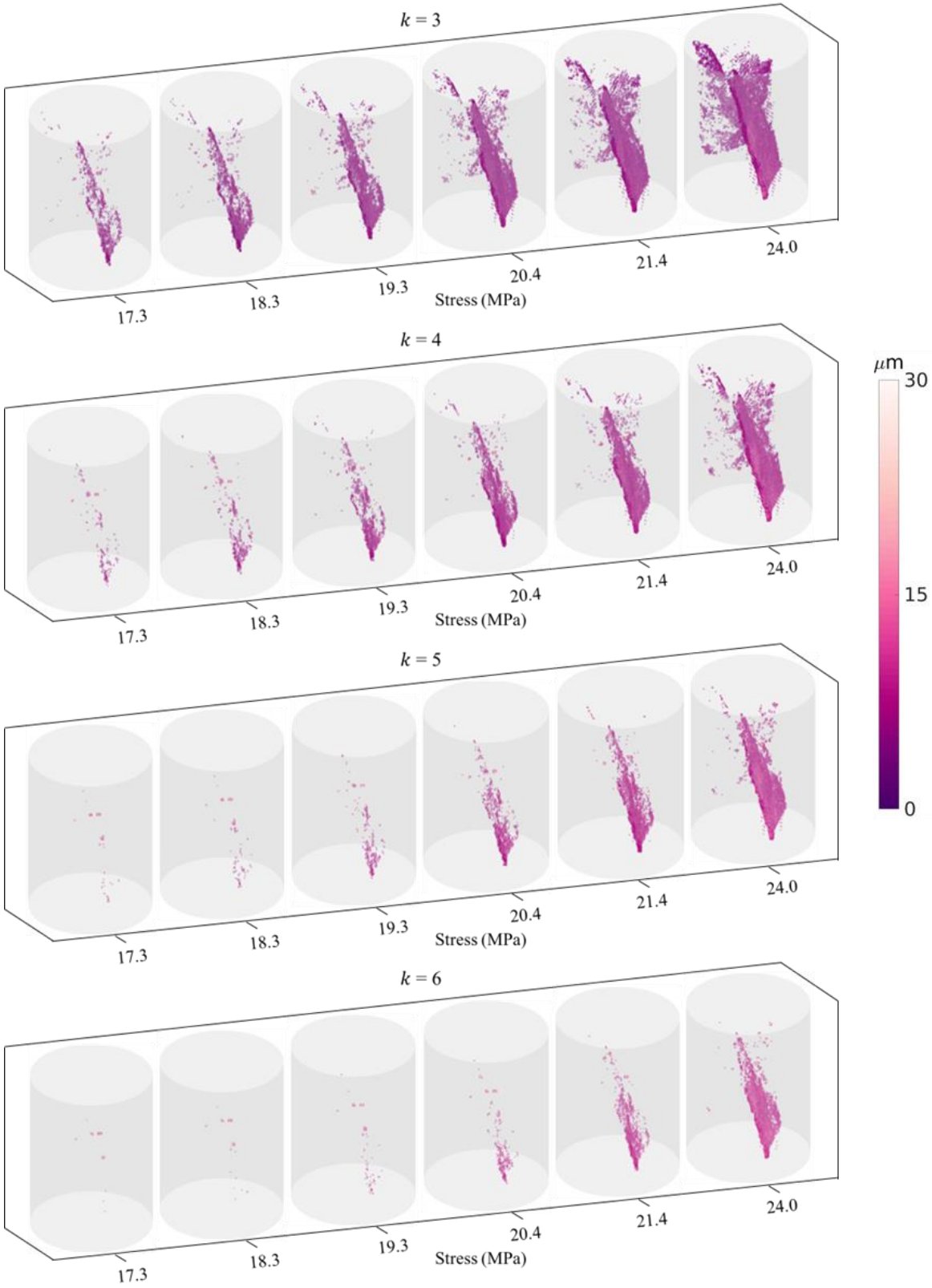
k = 3
17.3
18.3
19.3
20.4
21.4
24.0
Stress (MPa)
k = 4
17.3
18.3
19.3
20.4
21.4
24.0
Stress (MPa)
k = 5
17.3
18.3
19.3
20.4
21.4
24.0
Stress (MPa)
k = 6
17.3
18.3
19.3
20.4
21.4
24.0
Stress (MPa)
μm
30
15
0

Fig. 16

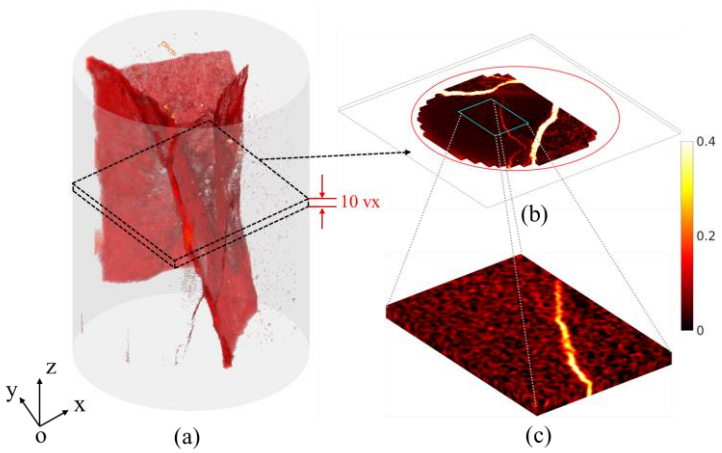

Fig. 17

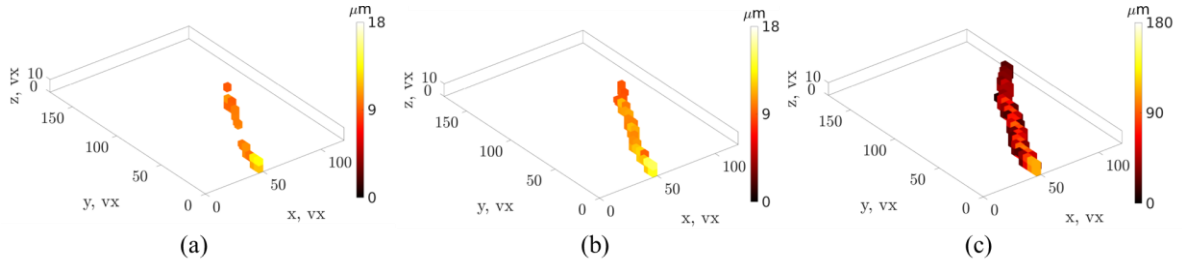
μm
18
9
0
z, vx
10
0
150
100
50
0
y, vx
0
50
100
x, vx
(a)
μm
18
9
0
z, vx
10
0
150
100
50
0
y, vx
0
50
100
x, vx
(b)
μm
180
90
0
z, vx
10
0
150
100
50
0
y, vx
0
50
100
x, vx
(c)

Fig. 18

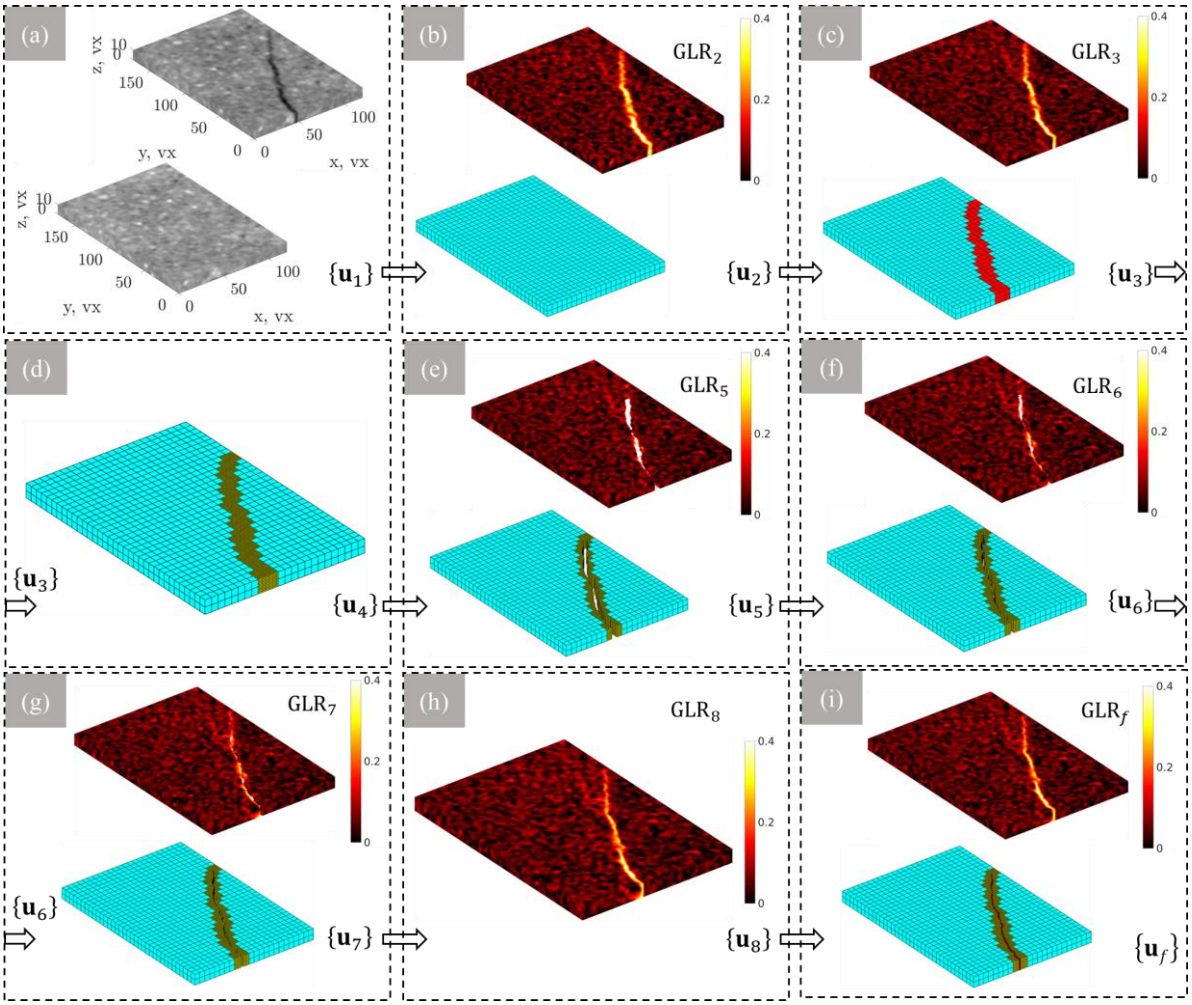
(a)
z, vx
y, vx
x, vx
$\{\mathbf{u}_1\}$
(b)
GLR_2
$\{\mathbf{u}_2\}$
(c)
GLR_3
$\{\mathbf{u}_3\}$
(d)
$\{\mathbf{u}_3\}$
$\{\mathbf{u}_4\}$
(e)
GLR_5
$\{\mathbf{u}_5\}$
(f)
GLR_6
$\{\mathbf{u}_6\}$
(g)
GLR_7
$\{\mathbf{u}_6\}$
$\{\mathbf{u}_7\}$
(h)
GLR_8
$\{\mathbf{u}_8\}$
(i)
GLR_f
$\{\mathbf{u}_f\}$

Fig. 19

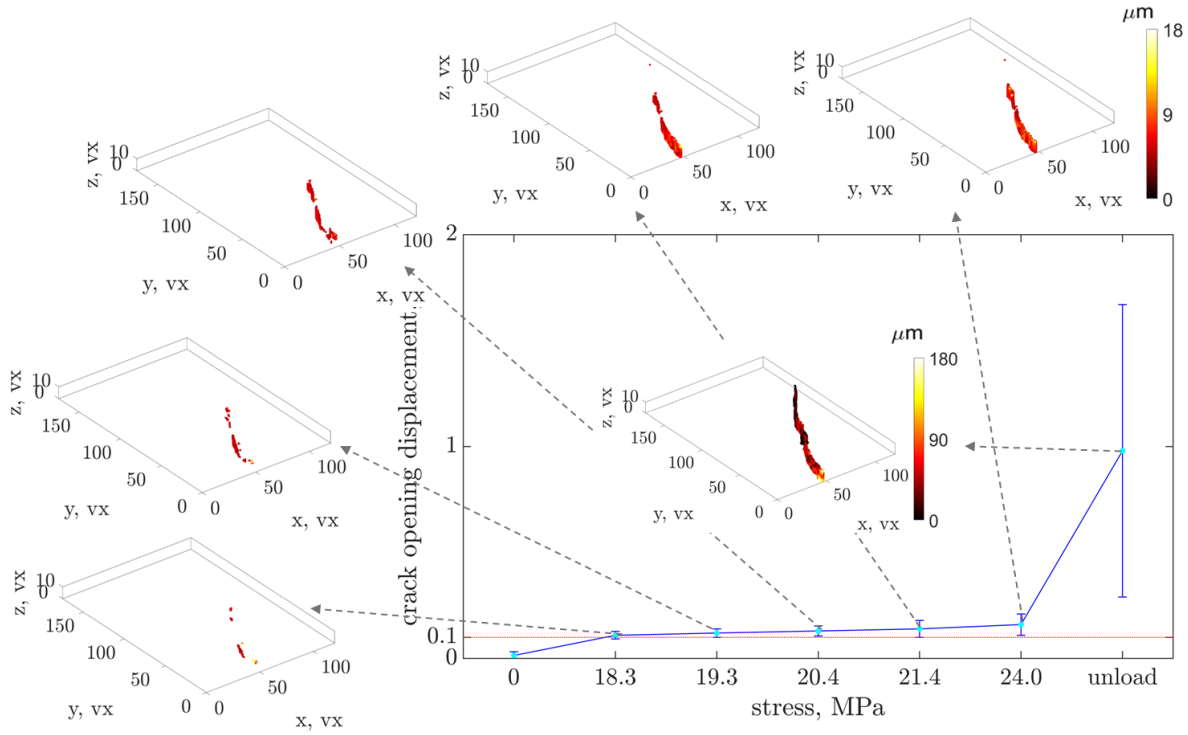
μm
18
9
0
μm
180
90
0
z, vx
y, vx
x, vx
crack opening displacement
stress, MPa
0
18.3
19.3
20.4
21.4
24.0
unload

Fig. 20

Table 1.

X-ray source	YXLON
Target / Anode	W (reflection mode)
Voltage	110 kV
Current	200 µA
Focal spot size	3×6 µm
Tube to detector	697 mm
Tube to object	140 mm
Detector	XRD 0822 AP14
Definition	1024×1024 pixels
Number of projections	720
Angular amplitude	360°
Frame average	No
Acquisition duration	25 min
Reconstruction algorithm	filtered back-projection
Gray levels amplitude	16 bits
Volume size	700 × 700 × 750 vx (after crop)
Field of view	32.2× 32.2 × 34.5 mm^3 (after crop)
Image scale	46.0 µm/ voxel
Pattern	natural (Figure 2)

Table 2.

axial stress (MPa)	17.3	18.3	19.3	20.4	21.4	24.0
V_D (mm^3)	61	107	315	1219	3129	7339
V_{COD} (%)	0.22	0.50	2.0	6.3	14.5	36.5
μ_{COD} (μm)	20.8	21.2	23.8	24.1	25.1	28.2
S_{COD} (μm)	2.8	2.8	3.2	4.1	4.2	6.1

Table 3.

axial stress (MPa)	18.3	19.3	20.4	21.4	24.0	unload
V_D (vx)	46	141	286	637	986	2070
V_{COD} (%)	2	7	14	31	48	100
μ_{COD} (μm)	5.1	5.5	6.0	6.5	7.5	40.9
S_{COD} (μm)	0.5	0.8	0.9	1.8	2.3	31.7